Multifunctional Additive (L-4-Fluorophenylalanine) for Efficient and Stable Inverted Perovskite Solar Cells

Jiabao Yang, Xingyu Pu, Tong Wang, Shuaici Cheng, Hui Chen, Qi Cao, Yixin Zhang, Ilhom Tojiboyev, Lioz Etgar, Hadi Salari, Fei Ye, and Xuanhua Li**

The harmful defects accumulated at surfaces and grain boundaries (GBs) limit the performance and stability of perovskite solar cells (PSCs), which results from the poor crystallization and ion migration. Here, a multifunctional molecular additive L-4-fluorophenylalanine (FPA) is explored for highly efficient and stable inverted PSCs. The multifunction is realized through comprehensive defect passivation, surface hydrophobicity, and crystallization control with the multitude groups, such as the amino and carbonyl groups for passivating the unsaturated lead defects at GBs, and the benzene ring for electron-deficient iodine defects, and the fluorine group for the improvement of crystallization and the inhibition of ions migration. The resulting inverted device shows a champion power conversion efficiency of 21.28% with negligible hysteresis. The unencapsulated FPA-modified devices maintain nearly 90% of the initial performance after high-temperature (85 °C) thermal accelerated aging for 500 h and 85% after aging for 4000 h under ambient conditions, and about 90% of the original efficiency after being maximum power point tracked for 1000 h under continuous illumination. This study provides a multipronged strategy to the future design of PSCs with higher efficiency and enhanced stability.

1. Introduction

In recent years, organic–inorganic halide perovskite materials (e.g., $CH_3NH_3PbI_3$, $MAPbI_3$, $MA = CH_3NH_3$) have attracted widespread attention in the scientific community due to the features of long carrier diffusion length, adjustable bandgap, a high absorption coefficient, and easy preparation.[1,2] After continuous exploration by researchers, the power conversion efficiency (PCE) of normal (n–i–p) PSCs exceeded 25%, and the inverted PSCs also reached 23.0% efficiency, which is comparable with traditional semiconductors and is expected to become a leader in the photovoltaic field.[3–7] Although PSCs are developing rapidly, their stability is still far from commercial standards.[8,9] Therefore, solving the inherent instability of perovskite materials is top priority, including thermal decomposition, ion migration, and crystal phase transformation of perovskite materials under extreme conditions. It is well known that the inherent volatility and poor thermal stability of the organic cation and halogen anion are some of the main reasons that affect the long-term stability of perovskite materials.[10–12] For example, the volatilization of organic components will leave PbI_2 or $Pb_{(0)}$, introducing carrier recombination centers and reducing the short-circuit current (J_{SC}) and fill factor (FF) of PSCs.[10] In addition, the decomposition of the perovskite is closely related to the grain boundaries (GBs), which are the main channels for ion migration and contain many dangling bonds that easily interact with moisture and oxygen.[13]

In response to this problem, interfacial engineering based on large hydrophobic polymers such as poly(methyl

---

J. Yang, X. Pu, T. Wang, H. Chen, Q. Cao, Y. Zhang, X. Li
State key Laboratory of Solidification Processing, Center for Nano Energy Materials, School of Materials Science and Engineering
Northwestern Polytechnical University
Xi'an 710072, P. R. China
E-mail: lixh32@nwpu.edu.cn

S. Cheng
Queen Mary University of London Engineering School
Northwestern Polytechnical University
Xi'an 710129, China

I. Tojiboyev
Institute Ion - Plasma and Laser Technologies
Uzbekistan Academy of Sciences
100125 Tashkent, Uzbekistan

L. Etgar
Institute of Chemistry, Casali Center for Applied Chemistry
The Hebrew University of Jerusalem
Jerusalem 91904, Israel

H. Salari
Faculty of Physical Chemistry
Shiraz University
Shiraz 71345, Iran

F. Ye
Institute of Optics
University of Rochester
New York, NY 14623, USA
E-mail: fye6@UR.Rochester.edu

The ORCID identification number(s) for the author(s) of this article can be found under https://doi.org/10.1002/solr.202101101.

DOI: 10.1002/solr.202101101

methacrylate)(PMMA),[14] polymer poly(4-vinylpyridine)(PVP),[15] conjugated polymers(PD-10-DTTE-7)[16] to patch GBs, the composition engineering of adjusting the composition of perovskite,[17–19] and additive engineering are widely used.[20–23] Among them, additive engineering is proved to be an effective way to obtain high-efficiency PSCs by improving the perovskite film quality without complicating fabrication processes, which is especially conducive to the large-scale manufacturing of PSCs. For example, Wang et al. introduced F127 block copolymer into the perovskite layer to passivate the defects at GBs,[24] but the perovskite grain refinement due to impurities and the poor conductivity of polymers are not advantageous for effective carrier transport. Therefore, small-molecule additives such as MACl,[25] phenylethylammonium iodide,[26] quaternary ammonium halides,[27] hypophosphorous acid,[28] benzoquinone[29] and 4-fluorophenethylamine[30–33] are used to passivate defects without deteriorating perovskite crystallization. However, most of the reported small-molecule additives contain few functional groups to achieve multipronged control (such as grain growth regulation, defect passivation, and stability enhancement).[34–36]

Here, we studied a multifunctional small molecule, L-4-fluorophenylalanine (FPA), and applied it for the first time in planar inverted PSCs. The effect of FPA on the crystallinity, defect density, and stability of the perovskite was systematically studied. It was revealed that the fluorine group in the molecule can inhibit the diffusion and migration of MA^+ ions and enhance the stability of the devices by forming a stable hydrogen bond with MA^+. In addition, the presence of the benzene ring can interact with I_2, and the amino and carbonyl groups can passivate the uncoordinated Pb^{2+} defect and inhibit the nonradiative recombination. In addition, the hydrophobic surface also contributes to stability improvement. As a result, a high-quality perovskite film has been obtained, and the PCE was increased from 17.87% to 21.28% with a very small hysteresis, J_{SC} of 23.15 mA cm^{-2}, and FF of 83.58%. It is worth noting that the stability of the optimized device has been significantly improved. The FPA-modified devices sustain about 90% of the original efficiency after maximum power point (MPP) tracking for 1000 h under continuous illumination at 45 °C. The PCE was 90% after continuous heating at 85 °C for 500 h in nitrogen environment and 85% after aging for 4000 h under ambient conditions.

2. Results and Discussion

Figure 1a shows the architecture of an inverted planar PSC, indium tin oxide (ITO)/NiO_x/perovskite/$PC_{61}BM + C_{60}$/BCP/Cr/Au ($PC_{61}BM$ represents [6,6]-phenyl-C_{61}-butyric acid methyl ester, and BCP represents 2,9-dimethyl-4,7-diphenyl-1,10-phenanthroline) and the structure of FPA. The FPA structure includes amino, carboxyl, and fluorine functional groups on the benzene ring, which are expected to have multivarious interactions with perovskites. We introduced FPA into the perovskite layer (termed MA/FPA) through additive engineering. We conducted high-resolution X-ray photoelectron spectroscopy (XPS) to understand the passivation mechanism of the FPA molecule. As shown in Figure S1, Supporting Information, compared with the XPS broad spectrum of the FPA molecule, a clear F1*s* peak in the broad spectrum of the MA/FPA film can be observed, which represents the successful introduction of FPA into the perovskite film. From the Pb spectrum, as shown in Figure 1b, we found that compared with the pure $MAPbI_3$ film, the two peaks of Pb

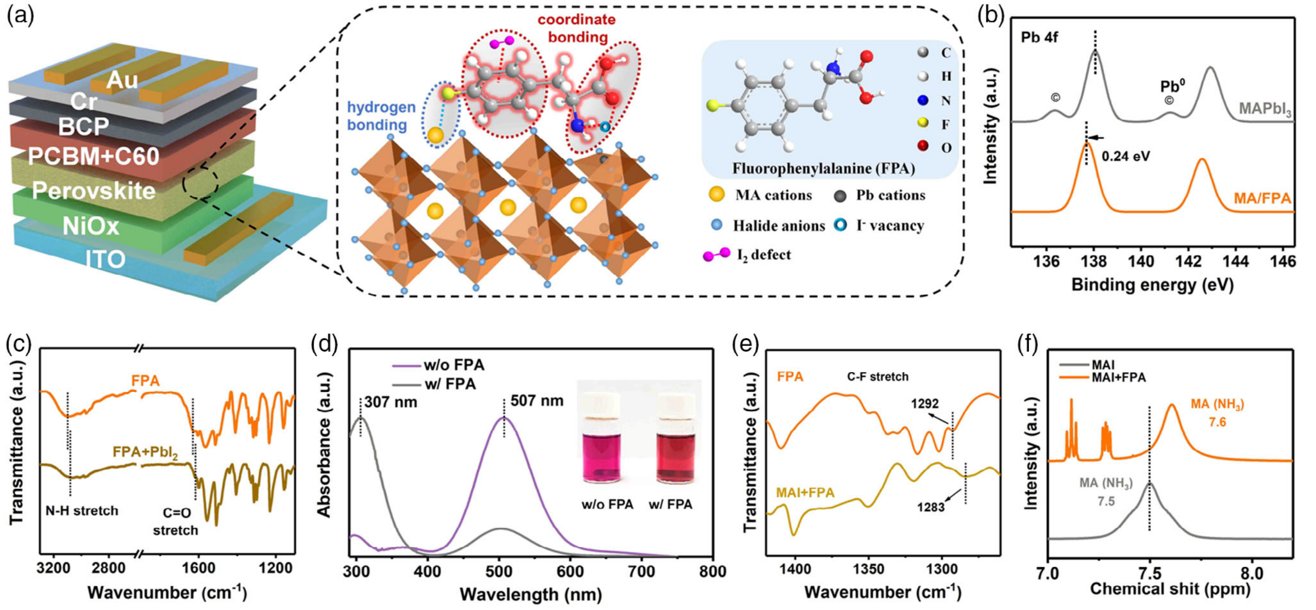

Figure 1. Research on the passivation mechanism of multifunctional molecule. a) Schematic showing the planar p–i–n device architecture (left) and the schematic showing the possible passivation mechanism of the L-4-fluorophenylalanine additive in the perovskite film (inner box). b) High-resolution XPS spectra of Pb 4*f* core level measured on the $MAPbI_3$ and MA/FPA films. c) FTIR spectra of FPA molecule and its mixture with lead iodide. d) UV–vis absorption spectra of iodine dissolved in different solvents in the range from 290 to 800 nm. Inset shows the photograph of iodine dissolved in the methylene chloride solution without and with 20% FPA (mass ratio). The concentration of iodine is 1 mg mL^{-1}. e) FTIR spectra of FPA and the mixture of FPA and MAI. f) ^{1}H NMR spectra of MA (NH_3) in MAI and the mixture of FPA and MAI.

$4f_{7/2}$ and Pb $4f_{5/2}$ in MA/FPA both shifted to the direction of low binding energy, indicating that the FPA molecule can compensate the Pb^{2+} defect in the perovskite. Moreover, the XPS spectrum of Pb 4*f* in the $MAPbI_3$ film shows two small shoulder peaks caused by Pb^0, which are due to the reduction of unsaturated Pb^{2+},[28] while the shoulder peaks disappeared after the introduction of FPA, proving that the unsaturated Pb^{2+} has been passivated, which has a positive effect on the carrier propagation efficiency.[37,38]

We further studied the interaction between FPA and perovskite through Fourier transform infrared (FTIR) spectra with the mixture of PbI_2 and FPA (1:1, mass ratio). In Figure 1c, it is observed that the infrared vibration peaks of the amino group ($–NH_2$) and carbonyl group (–COOH) in the FPA molecule both significantly redshifted, indicating the interaction of the lone electron pair on the amino group and the carboxyl group of FPA with PbI_2.

The unique large π-bond on the benzene ring gives it the property of electron donors that can passivate electron-deficient I_2 defects.[28,39] According to previous studies, the presence of residual I_2 in perovskite can introduce defects through the formation of I gaps or I–Pb inversion.[28] Here, we mixed I_2 and FPA to explore the possible interaction between I_2 and the benzene ring. The magenta methylene chloride solution of iodine turns darker after the addition of 20 wt% FPA, as shown in the inset of Figure 1d. The ultraviolet–visible (UV–vis) absorption spectra (Figure 1d) show a new absorption peak at 307 nm, which indicates the formation of benzene–iodine complex due to the electron-donating nature of the benzene ring.[39] Therefore, we speculate that the benzene ring can effectively reduce the density of electronic trap states caused by the presence of I_2 in the perovskite to improve the effectiveness of carrier transport in the device.

In addition, the fluorine group on the benzene ring can also contribute to the excellent passivation performance of FPA. We tested the FTIR spectra of the FPA molecule, MAI, and FPA + MAI mixture to analyze the possible interactions between the fluorine group and perovskites. In Figure 1e, the peak around 1292 cm^{-1} matches the C–F stretching vibration of FPA and shifts to a lower wavenumber of 1283 cm^{-1} in the MAI + FPA spectrum, indicating the interaction between MAI and FPA through the fluorine group.[40] We further conducted ^1H nuclear magnetic resonance (NMR), as shown in Figure 1f. The obvious signal at 7.5 ppm assigned to proton on NH_3^+ in MAI shifts to 7.6 ppm in the FPA + MAI mixture. The FTIR and NMR analyses reveal that the hydrogen bond is formed between fluorine group on FPA and NH_3^+ on MAI.[40–42]

The above analysis supports that FPA has the potential to passivate both the uncoordinated Pb^{2+} defects and the inevitable trace I_2 defects, and can also form hydrogen bonds with MA^+, which has a certain influence on the crystallization and stability of the perovskite. A schematic diagram of the multifarious interactions between the FPA molecule and perovskite is given in Figure 1a.

Figure 2a illustrates the schematic diagram of the preparation of perovskite films in detail. Through its interaction with perovskite, FPA inhibits the diffusion of MA^+ ions during perovskite film crystallization and induces the formation of high-quality perovskite film. A scanning electron microscope (SEM) was used to study the surface morphology and quality of the perovskite film. Figure 2b–c shows the top-view SEM images, the cross-sectional SEM images, and the crystal size distribution of $MAPbI_3$ film and MA/FPA film, respectively. It is observed from Figure 2b that the grains of the $MAPbI_3$ film are small (average grain diameter *D* is about 155.8 nm) and not uniform, and there are obvious cracks and residual PbI_2 (white particles). With the addition of the FPA multifunctional molecule, the grain size is enlarged, with an average size of about 260.5 nm, and the film is more compact and uniform with fewer GBs (Figure 2c).

The X-ray diffraction (XRD) further proved that the FPA molecule improved the quality of the perovskite film (Figure 2d–e). In Figure 2d, the modified perovskite film has no shifted diffractions or irrelevant diffractions to perovskite, indicating that the perovskite lattices were not affected by the additives. The peak around 12.8° corresponds to residual PbI_2, which is weakened in the FPA-contained perovskite film, suggesting that FPA suppressed the inadequate crystallization of PbI_2 and the decomposition of perovskite. Figure 2e shows an enlarged view of the (110) diffraction peaks of the perovskite film from 13.6° to 14.9°. With FPA in perovskite, the full-width-half-maximum (FWHM) of the diffraction peak of the (110) plane decreases, which may be related to the improvement of crystallinity and less scattering. This is consistent with the results of Raman spectroscopy (Figure S2, Supporting Information) and SEM (Figure 2b,c). Consistently, the UV–vis absorption of the MA/FPA film is also significantly enhanced (Figure 2f) due to the larger grain size of the perovskite, the reduction of GBs, and the improvement of the quality of the film.[13]

To verify the performance improvement of PSCs with FPA-modified perovskites, we fabricated PSCs with a structure of ITO/NiO_x/perovskite/$PC_{61}BM + C_{60}$/BCP/Cr/Au. The concentration of FPA in perovskite was optimized to be 0.2 mg mL^{-1} (Figure S3 and Table S1, Supporting Information). **Figure 3**a shows forward- and reverse-current density–voltage (*J*–*V*) curves of champion devices with $MAPbI_3$ and MA/FPA under 100 mW cm^{-2}, with the extracted parameters given in **Table 1**. At a reverse scan (RS) rate of 0.1 V s^{-1}, perovskite with FPA improves the PCE from 17.87% to 21.28%, with an open-circuit voltage (V_{OC}) from 1.07 to 1.10 V, a short-circuit current (J_{SC}) from 21.23 to 23.15 mA cm^{-2}, and FF from 78.68% to 83.58%. Figure S4, Supporting Information, shows the statistical distribution of photovoltaic parameters from ten devices, which reflects the excellent repeatability of the champion devices. The hysteresis factors (HF) of the devices are calculated using the formula $HF = (PCE_{reverse} - PCE_{forward})/PCE_{reverse})$.[43] Compared with the HF of the $MAPbI_3$ devices (4.48%), the HF of the MA/FPA devices is substantially reduced to 1.97%, suggesting the effective defect passivation and inhibition of ion migration for the perovskite with FPA additive. Figure 3b shows J_{SC} values obtained by the integration of the IPCE. The integrated currents of $MAPbI_3$ and MA/FPA devices are 20.44 and 22.12 mA cm^{-2}, respectively, which are well matched with the current values obtained from the *J*–*V* characteristics (error within 5%). Moreover, the champion devices of $MAPbI_3$ and MA/FPA were maintained at the MPP of 0.89 and 0.94 V, respectively, to track stable power output. In Figure 3c, the stabilized photocurrent of $MAPbI_3$ and MA/FPA is 19.32 and 22.29 mA cm^{-2}, corresponding to the stabilized PCE of 17.19% and 20.96%, respectively. The PSCs with FPA show a highly stable power output.

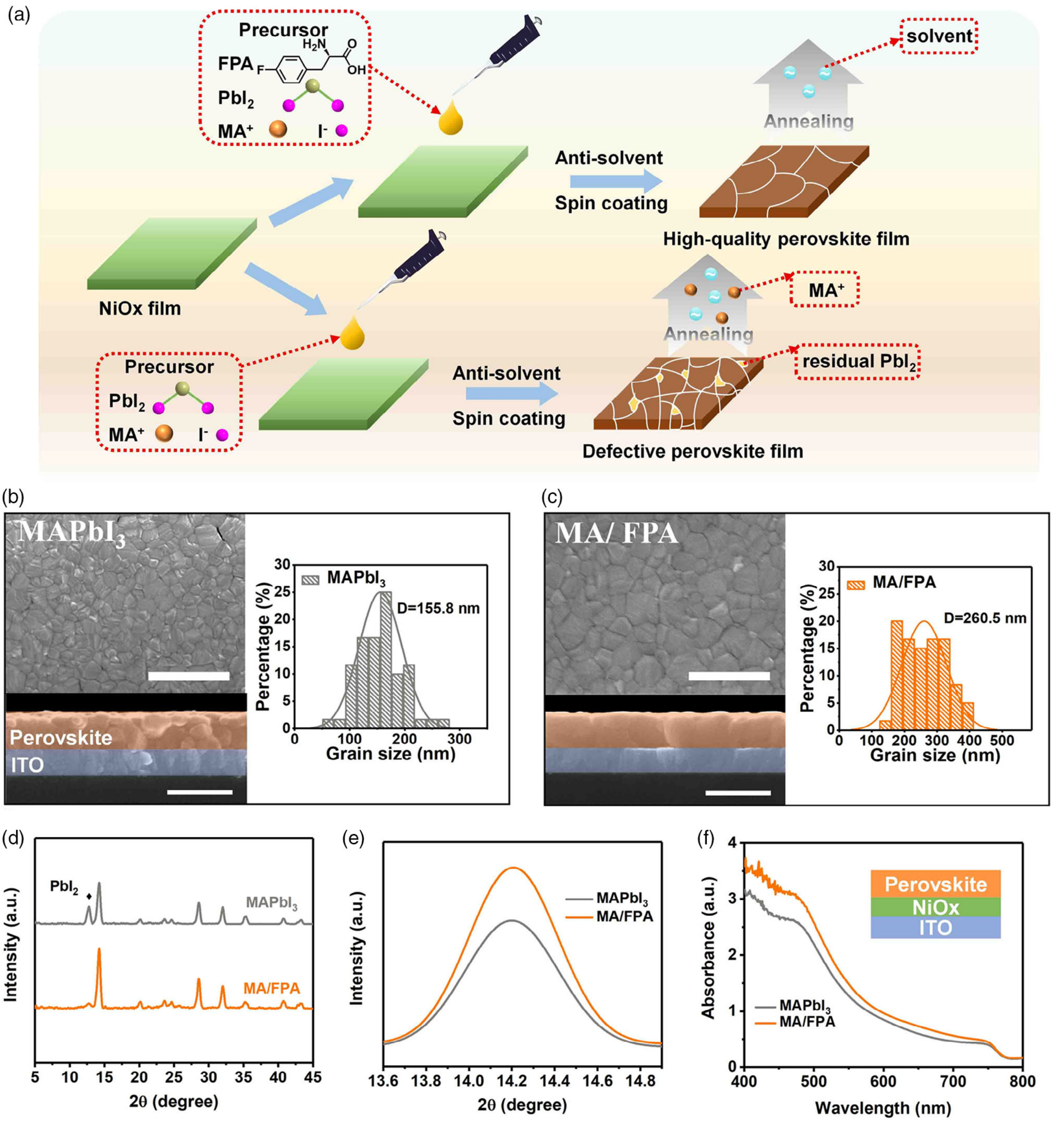

Figure 2. Microstructure and properties of perovskite films with and without multifunctional molecules. a) Schematic diagram of the preparation of perovskite films without and with FPA additive. b,c) SEM characterizations. Top-view and cross-sectional SEM images and grain size statistics (obtained from top-view SEM images) of $MAPbI_3$ (b) and MA/FPA films (c). The scales in top-view and cross-sectional SEM images are 1 μm and 500 nm, respectively. d) XRD patterns of these perovskite films and e) the zoom-in image of the 13.6–14.9 region. f) UV–vis absorption spectra of the perovskite films with and without multifunctional passivation molecules. The illustration shows the film structure used for testing.

To gain a deeper understanding of the charge-carrier dynamics, steady-state photoluminescence (PL) spectroscopy and time-resolved PL (TRPL) were studied, as shown in Figure 3d,e. Compared with the $MAPbI_3$ film, the MA/FPA exhibits a stronger band emission and a blueshift of 3 nm at the same excitation wavelength. We fit the TRPL curves with a biexponential decay function.[44,45] The results show that the average TRPL lifetime of the perovskite film with FPA is more than six times that

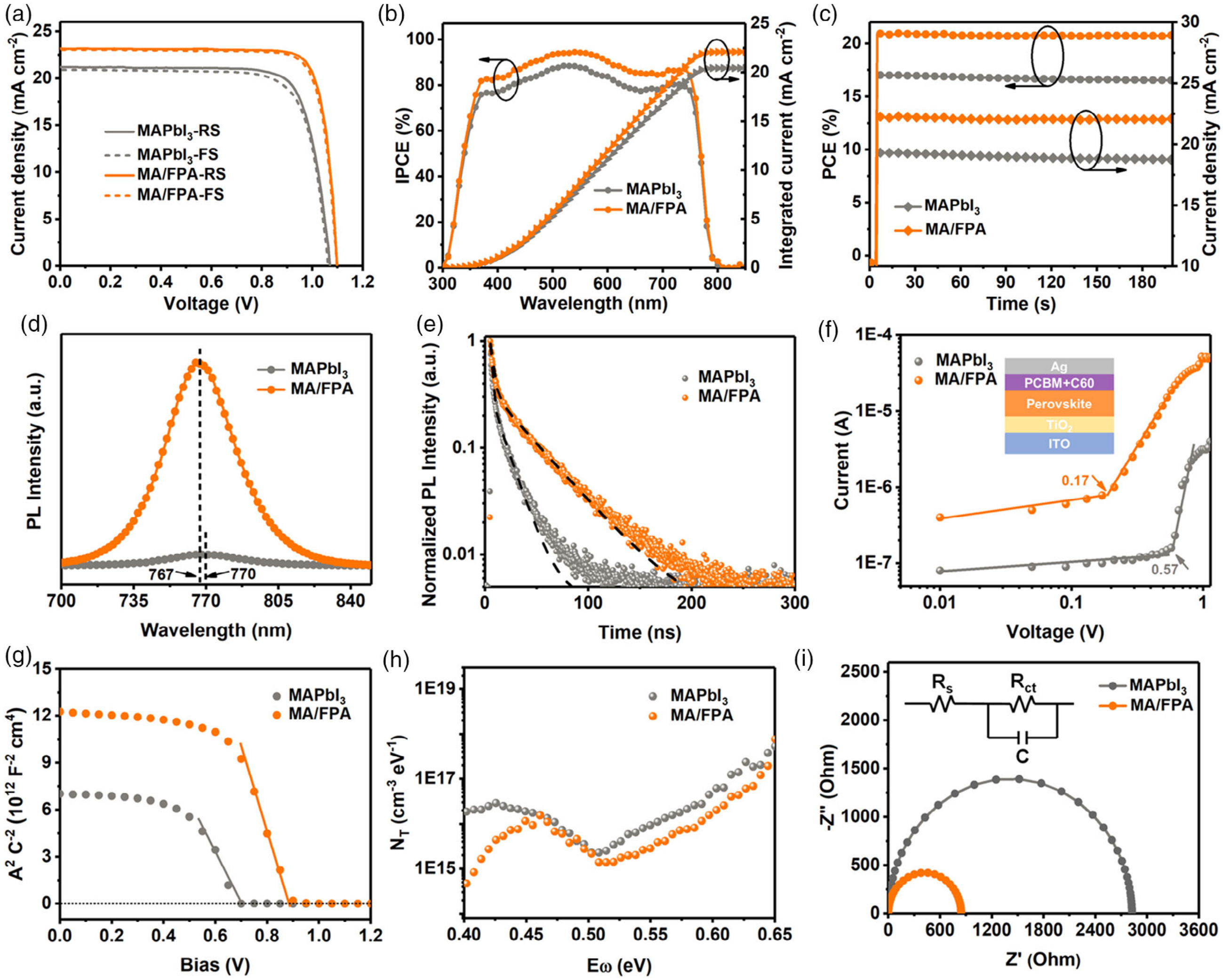

Figure 3. Photovoltaic properties of the devices. a) The $J-V$ curves of the champion devices based on $MAPbI_3$ and MA/FPA perovskite films in RS and forward scan (FS) under illumination of an AM 1.5 solar simulator (100 mW/cm^2). b) Corresponding IPCE curves and c) steady-state current densities and PCE of the PSCs measured at constant bias voltages. d) Steady-state and e) time-resolved PL spectra of the perovskite films deposited directly on the ITO glass substrate. f) The dark J–V curves of electron-only devices. The device architecture is shown in the inset. g) Mott–Schottky plots and h) tDOS spectra for the $MAPbI_3$ and MA/FPA PSCs. In A^2C^{-2}, A is the active area and C is the capacitance; N_T is trap state density; and E_ω represents the energetic defect level. i) Nyquist plots based on the EIS regarding the devices (inset: the equivalent circuit model of the devices).

of $MAPbI_3$ (3.63 ns), reaching 23.94 ns (Table S2, Supporting Information). A strong band emission, 3 nm blueshift in PL spectroscopy, and longer TRPL lifetime of the MA/FPA film provide strong evidence that FPA has good control on defects to reduce unnecessary nonradiation recombination and facilitate the conversion of light energy into electrical energy.[46]

We further studied the electrical properties of the devices to gain more insight into the effect on the device performance with FPA. The defect state density (N_{trap}) of the perovskite layer was studied by testing the J–V curves of the electron-only devices in the dark with the structure of ITO/TiO_2/perovskite/$PC_{61}BM + C_{60}$/Ag. The linear relationship in Figure 3f indicates an ohmic contact at a low bias voltage. When the bias voltage exceeds the inflection point, the current rapidly increases, indicating that the trap state is filled.[47,48] The voltage at the inflection point is called the limit voltage of trap filling (V_{TFL}). The measured V_{TFL} values for $MAPbI_3$ and MA/FPA are 0.57 V and 0.17 V, respectively. N_{trap} can be calculated by the following equation.

$$N_{trap} = 2\varepsilon\varepsilon_0 V_{TFL}/eL^2 \tag{1}$$

where e is the basic charge of the electron, L is the thickness of the perovskite film, ε is the relative permittivity of the perovskite, and ε_0 is the vacuum permittivity. In contrast to the $MAPbI_3$ device with a defect density of 2.02×10^{16} cm^{-3}, the device with FPA delivered a lower defect density of 6.02×10^{15} cm^{-3}. Thermal admittance spectroscopy (TAS) analysis was used to gain the quantification of the trap density of states (tDOS) by the following equations.[41]

Table 1. A summary of the reverse- and forward-scanning photovoltaic parameters and the calculated HF of the $MAPbI_3$ and MA/FPA devices under 100 mW cm^{-2} AM 1.5G illumination.

Devices	Scanning mode	V_{OC} [V]	J_{SC} [mA cm^{-2}]	FF [%]	PCE [%]	HF [%]
$MAPbI_3$	Reverse	1.07[a] (1.06)[b]	21.23 (20.97)	78.68 (78.06)	17.87 (17.35)	4.48[c]
	Forward	1.06 (1.06)	20.93 (20.66)	76.97 (76.40)	17.07 (16.67)	
MA/FPA	Reverse	1.10 (1.10)	23.15 (23.01)	83.58 (83.30)	21.28 (21.05)	1.97
	Forward	1.10 (1.10)	23.06 (22.84)	82.52 (82.21)	20.86 (20.66)	

[a] The best device performance from the different batch; [b] The average values of 10 devices from the different batch; [c] HF calculated from the optimal data of the reverse scanning.

$$N_T(E_\omega) = -\{V_{bi}\omega(dC/d\omega)\}/(qWk_BT) \tag{2}$$

$$E_\omega = k_BT\ln(\omega_0/\omega) \tag{3}$$

where C is the capacitance, ω is the angular frequency, ω_0 is the attempt-to-escape frequency, q is the elementary charge, k_B is the Boltzmann constant, and T is the temperature. V_{bi} and W are the built-in potential and depletion width, respectively, which were extracted from the Mott–Schottky analysis (Figure 3g). The density of deeper trap states (energy level above 0.40 eV) decreased after the introduction of the FPA molecule, as shown in Figure 3h. The decrease of the tDOS is consistent with the decreased photocurrent hysteresis, indicating the effective passivation of charge traps in the MA/FPA film.[49] Further, electrochemical impedance spectra (EIS) measurement reveals the positive effects of FPA molecule on the electron transport characteristics of PSCs.[50,51]The smaller charge transfer resistance (R_{ct}) is beneficial for the improvement of J_{SC} and FF, as shown in Figure 3i. The above results suggest that the FPA molecule can simultaneously control the negative effects of multiple defects, which maximizes the efficiency of carrier migration.

As long-term stability is one of the key issues for the practical application of PSCs, we conducted aging tests on the perovskite film in the air (RH = 40 ± 5%, heating at 85 °C for 24 h) to verify the extremely excellent stability of perovskite films with FPA. As shown in **Figure 4**a, after the rigorous test, the $MAPbI_3$ film was completely degraded (turned to yellow), while the MA/FPA film was dark. Therefore, the multifunctional molecular additive FPA can observably enhance the stability of the active layer through the powerful interaction with the perovskite, thereby improving the water and heat resistance of PSCs.

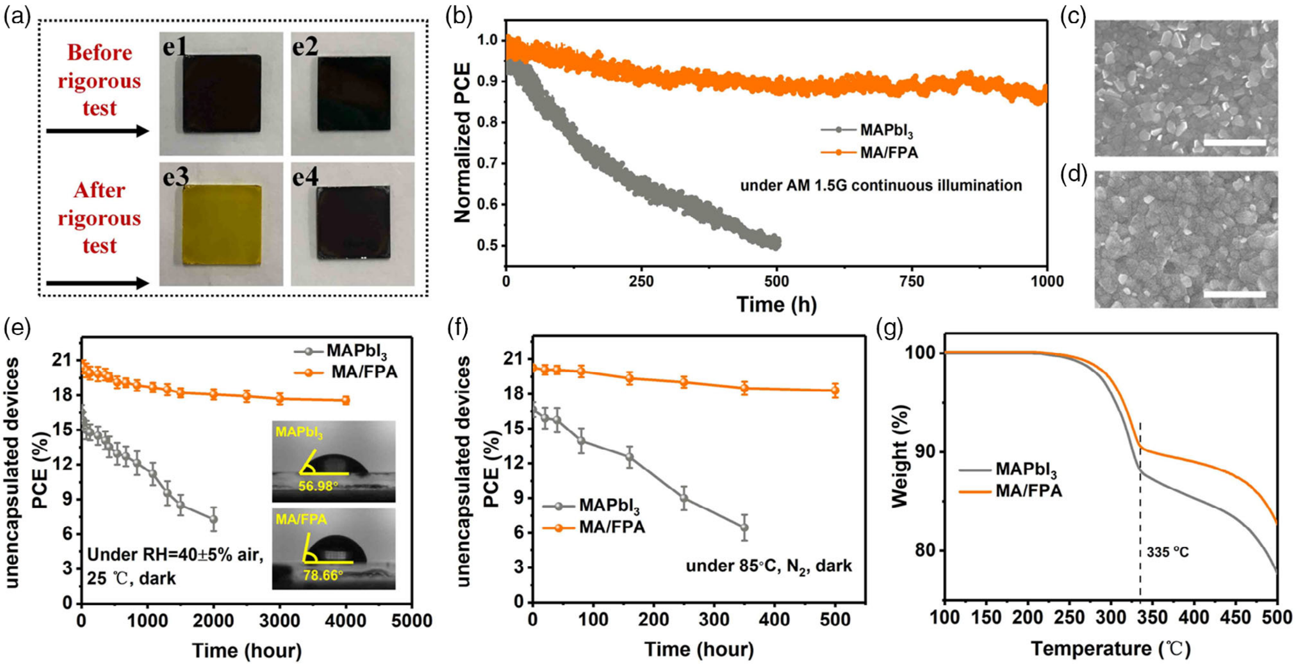

Figure 4. Stability testing of unencapsulated devices. a) Photographs of the $MAPbI_3$ (e1, e3) and MA/FPA (e2, e4) films before (e1, e2) and after (e3, e4) the "rigorous test," which refers to keeping the films in air environment (RH = 40% ± 5%) at 85 °C heating conditions for 24 h. b) The MPP tracking of the encapsulated device under 1 sun continuous illumination without a UV filter at 45 °C. The SEM images for c) $MAPbI_3$ and d) MA/FPA perovskite film after MPP tracking test. e) Statistical data on the PCE of unencapsulated devices varying with environmental storage time in the case of room temperature, darkness, and ambient air humidity of about 40% ± 5%. Inset: Contact angle of water on perovskite films. f) Monitoring the change of PCE with thermal aging time under the condition of continuous heating at 85 °C in nitrogen environment. g) The weight curve of perovskite films with and without FPA multifunctional molecule as a function of temperature.

The MPP tracking test of the encapsulated device under 1 sun continuous illumination without a UV filter at 45 °C shows that the PCE of MA/FPA devices remained at about 90% of the initial values after continuous illumination for 1000 h, while the PCE of $MAPbI_3$ decayed by 50% only after 500 h (Figure 4b). We observed the SEM images (Figure 4c,d) and XRD patterns (Figure S5, Supporting Information) of $MAPbI_3$ and MA/FPA films after the MPP tracking test (note: the perovskite film was obtained via peeling off the electrode with Kapton tape and spin coating chlorobenzene to remove electron transport layer). There is PbI_2 degraded from $MAPbI_3$ perovskite, while the MA/FPA perovskite displays a small amount of degraded PbI_2, which is consistent with the XRD patterns, indicating that FPA has a positive effect on keeping the perovskite composition stable. We studied the influence of the FPA molecule on the stability of unencapsulated PSCs through an environmental stability test in the air with a humidity of 40% ± 5% and a temperature of 25 °C for 4000 h (Figure 4e). The efficiency of the control device ($MAPbI_3$) quickly drops below 45% of the original efficiency within 2000 h, while the PCE of the MA/FPA devices can still retain about 85% of the initial efficiency after being placed for 4000 h. Further, the tDOS of the MA/FPA device after aging rarely changes (Figure S6, Supporting Information), which supports the device stability in the long term.

In addition, the surface hydrophobicity is another factor conducive to device stability. We dropped water droplets on the surface of the perovskite films to observed the water contact angle. It can be seen from the inset in Figure 4e that the contact angle of $MAPbI_3$ is 56.98°, while that of MA/FPA increased to 78.66°, which should be attributed to the vertical alignment of the hydrophobic benzene ring and fluorine group along the surface of the perovskite film caused by the interaction between amino group/carbonyl group in the FPA molecule and Pb via sharing the lone electron pair.[52] Increased hydrophobicity is beneficial to block the decomposition of the perovskite film under humidity and improve the environmental stability of the device.

To examine the thermal stability of the optimized perovskite material, we placed unencapsulated devices in a glove box filled with nitrogen and heated them continuously at 85 °C. The curves of PCE versus temperature are shown in Figure 4f. After continuous heating treatment for 500 h, the PCE of MA/FPA devices retained about 90% of the initial values, while the PCE of $MAPbI_3$ decayed by 60% only after heating for 350 h. The thermogravimetric analysis (TGA) in Figure 4g shows the decomposition temperature (DT) of $MAPbI_3$ at 305 °C (weight loss by 5%) while the DT of the perovskite with FPA increases to 314 °C. In addition, the organic component MAI sublimates around 335 °C,[53] whereas the perovskite with FPA molecule displays less weight loss due to the effective interaction between them. The increased DT and reduced weight loss explain the positive effect of FPA in improving the thermal stabilities of PSCs.

3. Conclusion

In summary, we provide an effective and simple method of perovskite passivation. FPA multifunctional alanine molecular additive with a special multigroup structure is explored to passivate both Pb^{2+} and I_2 defects, and control the perovskite crystallization, so as to achieve comprehensive effects of reducing defects, suppressing recombination, and greatly improving the quality of the perovskite film. The solution-treated planar inverted PSCs have a champion PCE of 21.28% and maintain about 90% of the initial efficiency after heating at 85 °C for 500 h under nitrogen atmosphere and 85% after 4000 h under ambient conditions. Moreover, the optimized device retains 90% after 1000 h under 1 sun illumination without a UV (ultraviolet) filter at 45 °C to track MPP. This method provides a strategy to improve the stability and efficiency of PSCs with multifunctional groups to enable the low-cost and large-scale fabrication for the commercialization of PSCs.

4. Experimental Section

Materials: Gamma-butyrolactone (GBL, 99.8%), anhydrous dimethyl sulfoxide (DMSO, 99.8%), chlorobenzene (CB, 99.8%), and isopropanol (IPA, 99.9%) were purchased from Sigma-Aldrich. Methylammonium iodide (MAI), lead iodide (PbI_2), [6,6]-phenyl-C61-butyric acid methyl ester (PCBM), and bathocuproine (BCP) were purchased from Xi'an Polymer Light Technology Corp. L-4-Fluorophenylalanine (FPA) was purchased from Aladdin. All materials were used without further purification.

Device Fabrication: The structure of the photovoltaic device was ITO/NiO_x/$MAPbI_3$ (or MA/FPA)/PCBM + C_{60}/BCP/Cr/Au. Indium tin oxide (ITO)-coated glass was cleaned with a cleaning detergent, and then deionized water, acetone, and ethanol solution were used for ultrasonic cleaning for 15 min, respectively. After nitrogen blowing to dry the cleaned ITO glass, the glass sheets were treated with ultraviolet ozone for 15 min to remove the organic residue and enhance the wettability. NiO_x was synthesized according to previous literature.[54] For the fabrication of hole transport layer of NiO_x, we spin coated the synthesized NiO_x aqueous solution on the ITO glass at 2000 rpm for 50 s in the air and heated at 100 °C for 10 min. Subsequently, the sample was transferred to a glove box filled with N_2. To make the $MAPbI_3$ precursor solution, MAI and PbI_2 were dissolved in 1 mL GBL/DMSO mixed solution (volume ratio of 7:3) with a molar ratio of 1:1 and stirred at 60 °C for 5 h.[55,56] To prepare MA/FPA precursor solution, different concentrations of FPA were added in $MAPbI_3$ precursor solution. Then, through one-step antisolvent method, the perovskite precursor was spin coated on NiO_x film at 1000 rpm for 10 s and 3000 rpm for 40 s, and chlorobenzene as the antisolvent solution was dropped on the film at the last 30 s during spin coating to remove the excess solvent. After annealing at 100 °C for 10 min, a perovskite film was obtained. Then $PC_{61}BM$ and C_{60} mixture solution (mass ratio, 4:1; 25 mg mL^{-1}) in chlorobenzene was spin coated on top of the perovskite film at 3000 rpm for 40 s and then annealed at 60 °C for 10 min. The BCP/IPA solution (0.5 mg mL^{-1}) was spin coated on $PC_{61}BM/C_{60}$ and annealed at 60 °C for 10 min to obtain the barrier layer. Finally, the chromium layer (4 nm) and gold layer (100 nm) were deposited under vacuum (4×10^{-6} mbar) by thermal evaporation. The effective area of the prepared device was 0.1 cm^2.[57]

Characterizations: The *J–V* curves were measured by a Keithley 2400 source meter with a scanning speed of 0.1 V s^{-1}. All devices were measured under AM 1.5G illumination (100 mW cm^{-2}) from a solar simulator (Newport 94023A Oriel Sol3A, Class AAA), using a Hamamatsu S1133 standard silicon diode to calibrate the luminous intensity.[58–60] The internal photo-to-current efficiency (IPCE) spectra were acquired in the wavelength range from 300 to 850 nm with Newport (1600 W). The steady-state PL spectra and TRPL of the samples were measured via a fluorescence spectrometer (Edinburgh Instruments, FLS980, excitation wavelength: 480 nm). A bias voltage of 0.8 V was applied to the electrochemical workstation (Chenhua 760), and the EIS of the devices were performed in dark in the frequency range from

0.1 Hz to 1 MHz, with the oscillation potential amplitude of 10 mV. The FTIR spectra were carried out by NICOLET iS50 FTIR spectrometer. X-ray photoelectron spectroscopy (XPS) spectra of the samples were tested by X-ray photoelectron spectrometer Axis Supra (Shimadzu Kratos) under a base pressure of 1×10^{-9} torr with a monochromatized Al Kα source and multichannel detector 452. The ultraviolet–visible (UV–vis) absorption spectra were obtained by a spectrophotometer (Lambda 35, Perkin-Elmer). The surface morphology of the perovskite films and the cross-sectional morphology of the samples were characterized by an field emission SEM (FESEM, FEI, NANOSEM450, US) with the working voltage of 10 kV. The XRD spectra of the samples were obtained by XRD-7000 using Cu Kα radiation (PANAlyticalX′pert PRO, $\lambda = 0.154$ nm) with a scanning speed of 5° min^{-1}. The Raman spectra of samples were tested by Horiba RENISHAW Via Raman. The TGA curves were acquired by STA 449F3 under nitrogen atmosphere with a heating rate of 5 °C min^{-1}. Water contact angle measurements were performed by DSA100 (KRUSS, Germany). The ^{1}H NMR spectrum (used DMSO-d_6 as locking solvent) was performed with Bruker AVANCE 400 MHz spectrometer.

Stability Test: The rigorous stability tests of the perovskite films were performed in an atmospheric environment (relative humidity of 40% ± 5%) and maintained a heating condition of 85 °C. The samples were not encapsulated to study their durability under severe conditions (oxygen, moisture, and high-temperature environment). The environmental stability of the devices was tested in an atmospheric environment with the relative humidity of 40% ± 5% and the temperature of 25 °C. The thermal stability was tested in a glove box filled with nitrogen and continuous heating on a heating table at 85 °C. All of the samples were tested without encapsulation. Heating in a nitrogen atmosphere was to eliminate the negative effects of oxygen, moisture, and only consider the changes in device performance with heating time. All devices were not further processed and the conditions were consistent with the *J*–*V* curve measurement. The operation stability of the encapsulated devices was tested under 1 sun continuous illumination without a UV filter at 45 °C to track the MPP via an MPP trace system (YH-VMPP-16). As for the encapsulation of devices in operational stability, it could be achieved via UV adhesive (LT-U001, Lumtec) and a glass on top.

Supporting Information

Supporting Information is available from the Wiley Online Library or from the author.

Acknowledgements

This research was supported by the National Natural Science Foundation of China (52172237 and 52072228), the Shaanxi International Cooperation Project (2020KWZ-018), the Shaanxi Science Fund for Distinguished Young Scholars (2022JC-21), the Research Fund of the State Key Laboratory of Solidification Processing (NPU), China (grant no. 2021-QZ-02), and the Fundamental Research Funds for the Central Universities (3102019JC005). The authors thank the members from the Analytical & Testing Center of Northwestern Polytechnical University for help with XPS and XRD characterization.

Conflict of Interest

The authors declare no conflict of interest.

Data Availability Statement

Research data are not shared.

Keywords

L-4-fluorophenylalanine, multifunctional groups, passivation, perovskite solar cells, stability

Received: December 29, 2021
Revised: February 13, 2022

---

[1] A. Kojima, K. Teshima, Y. Shirai, T. Miyasaka, *J. Am. Chem. Soc.* **2009**, *131*, 6050.
[2] M. M. Lee, J. Teuscher, T. Miyasaka, T. N. Murakami, H. J. Snaith, *Science* **2012**, *338*, 643.
[3] X. Li, S. Fu, W. Zhang, S. Ke, W. Song, J. Fang, *Sci. Adv.* **2020**, *6*, eabd1580.
[4] M. Du, X. Zhu, L. Wang, H. Wang, J. Feng, X. Jiang, Y. Cao, Y. Sun, L. Duan, Y. Jiao, K. Wang, X. Ren, Z. Yan, S. Pang, S. Liu, *Adv. Mater.* **2020**, *32*, 2004979.
[5] F. Wang, M. Yang, S. Yang, X. Qu, L. Yang, L. Fan, J. Yang, F. Rosei, *Nano Energy* **2020**, *67*, 104224.
[6] A. Al-Ashouri, E. Köhnen, B. Li, A. Magomedov, H. Hempel, P. Caprioglio, J. A. Márquez, A. B. Morales Vilches, E. Kasparavicius, J. A. Smith, N. Phung, D. Menzel, M. Grischek, L. Kegelmann, D. Skroblin, C. Gollwitzer, T. Malinauskas, M. Jošt, G. Matič, B. Rech, R. Schlatmann, M. Topič, L. Korte, A. Abate, B. Stannowski, D. Neher, M. Stolterfoht, T. Unold, V. Getautis, S. Albrecht, *Science* **2020**, *370*, 1300.
[7] C. Liang, H. Gu, Y. Xia, Z. Wang, X. Liu, J. Xia, S. Zuo, Y. Hu, X. Gao, W. Hui, L. Chao, T. Niu, M. Fang, H. Lu, H. Dong, H. Yu, S. Chen, X. Ran, L. Song, B. Li, J. Zhang, Y. Peng, G. Shao, J. Wang, Y. Chen, G. Xing, W. Huang, *Nat. Energy* **2020**, *6*, 38.
[8] Y. Rong, Y. Hu, A. Mei, H. Tan, M. I. Saidaminov, S. I. Seok, M. D. McGehee, E. H. Sargent, H. Han, *Science* **2018**, *361*, eaat8235.
[9] R. Wang, M. Mujahid, Y. Duan, Z.-K. Wang, J. Xue, Y. Yang, *Adv. Funct. Mater.* **2019**, *29*, 1808843.
[10] T. Leijtens, K. Bush, R. Cheacharoen, R. Beal, A. Bowring, M. D. McGehee, *J. Mater. Chem. A* **2017**, *5*, 11483.
[11] G. Niu, W. Li, F. Meng, L. Wang, H. Dong, Y. Qiu, *J. Mater. Chem. A* **2014**, *2*, 705.
[12] C. Chen, Z. Song, C. Xiao, D. Zhao, N. Shrestha, C. Li, G. Yang, F. Yao, X. Zheng, R. J. Ellingson, C.-S. Jiang, M. Al-Jassim, K. Zhu, G. Fang, Y. Yan, *Nano Energy* **2019**, *61*, 141.
[13] A.-F. Castro-Méndez, J. Hidalgo, J.-P. Correa-Baena, *Adv. Energy Mater.* **2019**, *9*, 1901489.
[14] J. Peng, J. I. Khan, W. Liu, E. Ugur, T. Duong, Y. Wu, H. Shen, K. Wang, H. Dang, E. Aydin, X. Yang, Y. Wan, K. J. Weber, K. R. Catchpole, F. d. r. Laquai, S. De Wolf, T. P. White, *Adv. Energy Mater.* **2018**, *8*, 1801208.
[15] L. Zuo, H. Guo, D. W. deQuilettes, S. Jariwala, N. De Marco, S. Dong, R. A.-O. DeBlock, D. A.-O. Ginger, B. A.-O. Dunn, M. Wang, Y. Yang, *Sci. Adv.* **2017**, *3*, e1700106.
[16] X.-X. Gao, D.-J. Xue, D. Gao, Q. Han, Q.-Q. Ge, J.-Y. Ma, J. Ding, W. Zhang, B. Zhang, Y. Feng, G. Yu, J.-S. Hu, *Sol. RRL* **2019**, *3*, 1800232.
[17] J. C. Dahl, W. T. Osowiecki, Y. Cai, J. K. Swabeck, Y. Bekenstein, M. Asta, E. M. Chan, A. P. Alivisatos, *Chem. Mater.* **2019**, *31*, 3134.
[18] T. Matsui, T. Yamamoto, T. Nishihara, R. Morisawa, T. Yokoyama, T. Sekiguchi, T. Negami, *Adv. Mater.* **2019**, *31*, 1806823.
[19] T. Singh, T. Miyasaka, *Adv. Energy Mater.* **2018**, *8*, 1700677.
[20] Y. Zhao, P. Zhu, M. Wang, S. Huang, Z. Zhao, S. Tan, T. H. Han, J. W. Lee, T. Huang, R. Wang, J. Xue, D. Meng, Y. Huang, J. Marian, J. Zhu, Y. Yang, *Adv. Mater.* **2020**, *32*, e1907769.

[21] J. Zhu, B. He, Z. Gong, Y. Ding, W. Zhang, X. Li, Z. Zong, H. Chen, Q. Tang, *ChemSusChem* **2020**, *13*, 1834.
[22] J. Jiang, X. Fang, Y. Xu, X. Jia, Y. Chen, Y. Chen, H. Hu, N. Yuan, J. Ding, *ChemSusChem* **2020**, *13*, 412.
[23] Z. Wu, M. Jiang, Z. Liu, A. Jamshaid, L. K. Ono, Y. Qi, *Adv. Energy Mater.* **2020**, *10*, 1903696.
[24] C. Wang, Z. Song, D. Zhao, R. A. Awni, C. Li, N. Shrestha, C. Chen, X. Yin, D. Li, R. J. Ellingson, X. Zhao, X. Li, Y. Yan, *Sol. RRL* **2019**, *3*, 1900078.
[25] S. Zheng, G. Wang, T. Liu, L. Lou, S. Xiao, S. Yang, *Sci. China Chem.* **2019**, *62*, 800.
[26] Y. Zhang, S. Jang, I. W. Hwang, Y. K. Jung, B. R. Lee, J. H. Kim, K. H. Kim, S. H. Park, *ACS Appl. Mater. Interfaces* **2020**, *12*, 24827.
[27] X. Zheng, B. Chen, J. Dai, Y. Fang, Y. Bai, Y. Lin, H. Wei, X. C. Zeng, J. Huang, *Nat. Energy* **2017**, *2*, 17102.
[28] W. Zhang, S. Pathak, N. Sakai, T. Stergiopoulos, P. K. Nayak, N. K. Noel, A. A. Haghighirad, V. M. Burlakov, D. W. deQuilettes, A. Sadhanala, W. Li, L. Wang, D. S. Ginger, R. H. Friend, H. J. Snaith, *Nat. Commun.* **2015**, *6*, 10030.
[29] C. Qin, T. Matsushima, T. Fujihara, C. Adachi, *Adv. Mater.* **2017**, *29*, 1603808.
[30] Y. Wei, P. Audebert, L. Galmiche, J. S. Lauret, E. Deleporte, *J. Phys. D: Appl. Phys.* **2013**, *46*, 135105.
[31] Y. Wei, J. S. Lauret, L. Galmiche, P. Audebert, E. Deleporte, *Opt. Express* **2012**, *20*, 10399.
[32] Y. Wei, P. Audebert, L. Galmiche, J.-S. Lauret, E. Deleporte, *Materials* **2014**, *7*, 4789.
[33] S. Zhang, G. Lanty, J.-S. Lauret, E. Deleporte, P. Audebert, L. Galmiche, *Acta Mater.* **2009**, *57*, 3301.
[34] C. Cui, D. Xie, P. Lin, H. Hu, S. Che, K. Xiao, P. Wang, L. Xu, D. Yang, X. Yu, *Sol. Energy Mater. Sol. Cells* **2020**, *208*, 110435.
[35] Y. Li, J. Shi, J. Zheng, J. Bing, J. Yuan, Y. Cho, S. Tang, M. Zhang, Y. Yao, C. F. J. Lau, D. S. Lee, C. Liao, M. A. Green, S. Huang, W. Ma, A. W. Y. Ho-Baillie, *Adv. Sci.* **2020**, *7*, 1903368.
[36] A. Solanki, M. M. Tavakoli, Q. Xu, S. S. H. Dintakurti, S. S. Lim, A. Bagui, J. V. Hanna, J. Kong, T. C. Sum, *Adv. Mater.* **2020**, *32*, 1907864.
[37] Y. Gao, Y. Wu, Y. Liu, C. Chen, X. Bai, L. Yang, Z. Shi, W. W. Yu, Q. Dai, Y. Zhang, *ACS Appl. Mater. Interfaces* **2020**, *12*, 3631.
[38] A. Ghosh, D. K. Chaudhary, A. Mandal, S. Prodhan, K. K. Chauhan, S. Vihari, G. Gupta, P. K. Datta, S. Bhattacharyya, *J. Phys. Chem. Lett.* **2020**, *11*, 591.
[39] Z.-b. Liu, J. Tian, W. Zang, W.-Y. Zhou, F. Song, C.-P. Zhang, J.-Y. Zheng, H. Xu, *Opt. Lett.* **2004**, *29*, 1099.
[40] J. Yang, C. Liu, C. Cai, X. Hu, Z. Huang, X. Duan, X. Meng, Z. Yuan, L. Tan, Y. Chen, *Adv. Energy Mater.* **2019**, *9*, 1900198.
[41] N. Li, S. Tao, Y. Chen, X. Niu, C. K. Onwudinanti, C. Hu, Z. Qiu, Z. Xu, G. Zheng, L. Wang, Y. Zhang, L. Li, H. Liu, Y. Lun, J. Hong, X. Wang, Y. Liu, H. Xie, Y. Gao, Y. Bai, S. Yang, G. Brocks, Q. Chen, H. Zhou, *Nat. Energy* **2019**, *4*, 408.
[42] G. Liu, X.-X. Xu, S. Xu, L. Zhang, H. Xu, L. Zhu, X. Zhang, H. Zheng, X. Pan, *J. Mater. Chem. A* **2020**, *8*, 5900.
[43] S. N. Habisreutinger, N. K. Noel, H. J. Snaith, *ACS Energy Lett.* **2018**, *3*, 2472.
[44] Z. Yang, J. Xie, V. Arivazhagan, K. Xiao, Y. Qiang, K. Huang, M. Hu, C. Cui, X. Yu, D. Yang, *Nano Energy* **2017**, *40*, 345.
[45] R. K. Ahrenkiel, *Solid-State Electron.* **1992**, *35*, 239.
[46] S. Yuan, F. Qian, S. Yang, Y. Cai, Q. Wang, J. Sun, Z. Liu, S. F. Liu, *Adv. Funct. Mater.* **2019**, *29*, 1807850.
[47] Y. Zhao, H. Tan, H. Yuan, Z. Yang, J. Z. Fan, J. Kim, O. Voznyy, X. Gong, L. N. Quan, C. S. Tan, J. Hofkens, D. Yu, Q. Zhao, E. H. Sargent, *Nat. Commun.* **2018**, *9*, 1607.
[48] Y. Liu, Z. Yang, D. Cui, X. Ren, J. Sun, X. Liu, J. Zhang, Q. Wei, H. Fan, F. Yu, X. Zhang, C. Zhao, S. F. Liu, *Adv. Mater.* **2015**, *27*, 5176.
[49] Y. Shao, Z. Xiao, C. Bi, Y. Yuan, J. Huang, *Nat. Commun.* **2014**, *5*, 5784.
[50] W. Zhang, A. Sadollahkhani, Y. Li, V. Leandri, J. M. Gardner, L. Kloo, *ACS Appl. Energy Mater.* **2019**, *2*, 2723.
[51] S. Teo, Z. Guo, Z. Xu, C. Zhang, Y. Kamata, S. Hayase, T. Ma, *ChemSusChem* **2019**, *12*, 518.
[52] S. Wang, Z. Li, Y. Zhang, X. Liu, J. Han, X. Li, Z. Liu, S. Liu, W. C. H. Choy, *Adv. Funct. Mater.* **2019**, *29*, 1900417.
[53] A. Dualeh, P. Gao, S. I. Seok, M. K. Nazeeruddin, M. Graetzel, *Chem. Mater.* **2014**, *26*, 6160.
[54] S. Bai, P. Da, C. Li, Z. Wang, Z. Yuan, F. Fu, M. Kawecki, X. Liu, N. Sakai, J. T.-W. Wang, S. Huettner, S. Buecheler, M. Fahlman, F. Gao, H. J. Snaith, *Nature* **2019**, *571*, 245.
[55] J. Wang, W. Fu, S. Jariwala, I. Sinha, A. K. Y. Jen, D. S. Ginger, *ACS Energy Lett.* **2018**, *4*, 222.
[56] H. Tang, Q. Cao, Z. He, S. Wang, J. Han, T. Li, B. Gao, J. Yang, D. Deng, X. Li, *Sol. RRL* **2019**, *4*, 1900415.
[57] S. Wang, B. Yang, J. Han, Z. He, T. Li, Q. Cao, J. Yang, J. Jiajia, X. Li, Z. Liu, S. F. Liu, C. Tang, A. Hagfeldt, *Energy Environ. Sci.* **2020**, *13*, 5068.
[58] J. Han, S. Wang, X. Li, H. Tang, Q. Cao, J. Yang, J. Zhu, X. Liu, Z. Li, W. Liu, *Sol. RRL* **2019**, *3*, 1900133.
[59] Y. Xie, X. Wang, Q. Chen, S. Liu, Y. Yun, Y. Liu, C. Chen, J. Wang, Y. Cao, F. Wang, T. Qin, W. Huang, *Macromolecules* **2019**, *52*, 4757.
[60] J. Han, S. Wang, J. Yang, S. Guo, Q. Cao, H. Tang, X. Pu, B. Gao, X. Li, *ACS Appl. Mater. Interfaces* **2020**, *12*, 4970.